frontiers in Earth Science

ORIGINAL RESEARCH
published: 21 April 2021
doi: 10.3389/feart.2021.665610

Petrogenesis of the Cretaceous Intraplate Mafic Intrusions in the Eastern Tianshan Orogen, NW China

Weifeng Zhang[1,2], Xin Deng[1], Bing Tu[1], Lianhong Peng[1] and Xinbiao Jin[2]*

[1] Wuhan Center of China Geological Survey, Wuhan, China, [2] Research Center for Petrogenesis and Mineralization of Granitoids, Wuhan, China

In this study, we conducted zircon U-Pb dating, and whole-rock geochemical and Sr-Nd isotope analyses on the Late Mesozoic dolerite dykes in the Bailingshan Fe deposit (Eastern Tianshan Orogen, NW China) to unravel their petrogenesis and regional tectonic significance. Zircon U-Pb dating on the dolerite yielded an Early Cretaceous age of 129.7 ± 1.4 Ma. The dolerite is calc-alkaline sodic (Na_2O/K_2O = 4.71 to 6.80), and enriched in LILEs (Rb, K, Sr, and Pb) but depleted in HFSEs (Nb, Ta, and Ti). The intermediate Nb/U (16.7 to 18.5) and Ce/Pb (6.33 to 6.90) values, and the presence of xenocrystic zircons in these dolerite dykes suggest crustal assimilation during the magma evolution. Petrological modeling suggests fractionation of olivine, pyroxene, garnet, and spinel. All the dolerite samples have low initial $^{87}Sr/^{86}Sr$ (0.7041 to 0.7043) and positive $\varepsilon_{Nd}(t)$ (+ 4.6 to + 5.1) values, indicative of a depleted asthenospheric mantle source. Partial melting modeling suggests that the melting has occurred in the spinel-garnet stability field. Integrating the data from ore deposit geology, geochronology, geochemistry and Sr-Nd isotopes, we proposed that the Late Cretaceous Eastern Tianshan mafic magmatism was developed in an intraplate extension setting.

Keywords: petrogenesis, asthenospheric melts, within-plate magmatism, late mesozoic, eastern tianshan

OPEN ACCESS

Edited by:
Sean C. Johnson, University College Dublin, Ireland

Reviewed by:
Qiang Ma, China University of Geosciences Wuhan, China
Jinsheng Han, China University of Geosciences Wuhan, China

****Correspondence:***
Xin Deng
cugxd@163.com

Specialty section:
This article was submitted to Petrology, a section of the journal Frontiers in Earth Science

Received: *08 February 2021*
Accepted: *31 March 2021*
Published: *21 April 2021*

Citation:
Zhang W, Deng X, Tu B, Peng L and Jin X (2021) Petrogenesis of the Cretaceous Intraplate Mafic Intrusions in the Eastern Tianshan Orogen, NW China. Front. Earth Sci. 9:665610. doi: 10.3389/feart.2021.665610

INTRODUCTION

The Eastern Tianshan Orogen is located between the Tarim and Junggar blocks (Mao et al., 2005; Han et al., 2010; Wang et al., 2014; Hou et al., 2014). Devonian to Triassic igneous rocks are widely exposed in the orogen, consisting of the Jingerquan granite (376.9 ± 3.1 Ma), Bailingshan granitoids (317 to 307 Ma), Huangshandong mafic-ultramafic intrusions (274 ± 3 Ma), and Donggebi granite porphyry (233.8 ± 2.5 Ma) (Zhou et al., 2010; Deng et al., 2015; Zhang et al., 2015, 2016; Zhao et al., 2019). Since many of these intrusions are related to regional magmatic-hydrothermal mineralization, several studies were conducted to understand their geochronology, petrogenesis, and geodynamic setting (Zhang et al., 2015, 2016; Xiao et al., 2017; Zhao et al., 2019), which suggested that the Devonian-Carboniferous intrusions are arc-related, whereas the Permian-Triassic intrusions are syn- to post-collisional (Wu et al., 2006; Zhou et al., 2010; Wang et al., 2014; Zhao et al., 2019). However, the Late Mesozoic tectonic setting is still poorly constrained due to the lack of robust indicator, which inhibits the reconstruction of the completed geological history for the Eastern Tianshan Orogen.

Geochemistry of basaltic magmas is an effective geodynamic tracer, because basalts from different tectonic settings have distinctive geochemical characteristics (Pearce, 1982, 2014; Wilson, 1989;

Xia and Li, 2019). For instance, oceanic island basalts (OIB) are enriched in light rare earth elements (LREEs) and high field strength elements (HFSEs), whereas arc-related basalts are characterized by low Nb/La ratios and negative Nb, Ta, and Ti anomalies, and mid-ocean ridge basalts (MORB) have high contents of compatible trace elements and depleted isotopic values (Sun and McDonough, 1989; Hofmann, 1997). In the past decades, a large number of tectonic discrimination diagrams were established using basalt geochemistry (Pearce and Norry, 1979, Pearce, 1982, 2008; Wood, 1980; Shervais, 1982; Mullen, 1983; Meschede, 1986; Vermeesch, 2006; Ross and Bedard, 2009; Ishizuka et al., 2014; Saccani, 2015). Recent review studies suggested that intraplate basalts can be distinguished from arc-related ones by Zr-Zr/Y and Th/Yb-Ta/Yb diagrams, whereas OIB and MORB are distinguishable from each other in the ternary 3Tb-Th-2Ta diagram (Xia and Li, 2019).

In this contribution, we describe the newly-discovered Cretaceous dolerite dykes near the Bailingshan deposit in the Eastern Tianshan, and present their whole-rock geochemical and isotopic compositions. These dolerite dykes represent the youngest magmatic rocks in the Eastern Tianshan, and our data provide new petrogenetic insight and improve our understanding in the Late Mesozoic tectonic evolution of the region.

REGIONAL GEOLOGY

The Chinese Eastern Tianshan in NE Xinjiang (NW China) is an important component of the Central Asian Orogenic Belt (CAOB). The prolonged arc magmatism and collisional orogenesis have formed the widespread Paleozoic to Permian magmatic rocks and numerous Fe, Cu-Ni, Au-Ag, Pb-Zn and Mo deposits (Mao et al., 2005; Han et al., 2010; Wang et al., 2014; Hou et al., 2014; Li et al., 2019). From north to south, the Eastern Tianshan comprises four tectonic terranes, including the Dananhu-Tousuquan arc belt, Kanggur shear zone, Aqishan-Yamansu belt and the Central Tianshan block (**Figure 1**; Qin et al., 2002; Mao et al., 2005). These tectonic terranes are bounded by several roughly E-W trending faults, including the Kanggur, Yamansu and Aqikekuduke (Chen and Jahn, 2004; Mao et al., 2005; Xiao et al., 2008; Yang et al., 2009).

The northern Dananhu-Tousuquan island arc belt contains predominantly Silurian to Carboniferous calc-alkaline felsic lavas, mafic volcanic-volcanoclastic rocks and marine clastic sediments (Mao et al., 2005; Zhang et al., 2015). Overlying these sedimentary-volcanic rocks are Permian basalts and Cenozoic sediments. Many Devonian to Carboniferous (ca. 360 – 320 Ma) intrusions were considered to be arc-related (Wu et al., 2006; Zhou et al., 2010; Wang et al., 2014). Several important porphyry copper deposits (PCDs) were discovered along this belt, notably Tuwu, Yandong, Yuhai, and Linglong (Shen et al., 2014; Xiao et al., 2017; Wang et al., 2018). The Kanggur shear zone (about 400 km long and 20 km wide) contains dominantly Carboniferous volcaniclastic rocks, clastic rocks and ophiolite fragments, most of which are ductile deformed (Mao et al., 2005; Li et al., 2006). Abundant Permian mafic-ultramafic intrusions and important Cu-Ni sulfide deposits were formed in the eastern Kanggur shear zone (Han et al., 2010; Zhang et al., 2012; Deng et al., 2015). Besides, some syn- or post-collisional-related

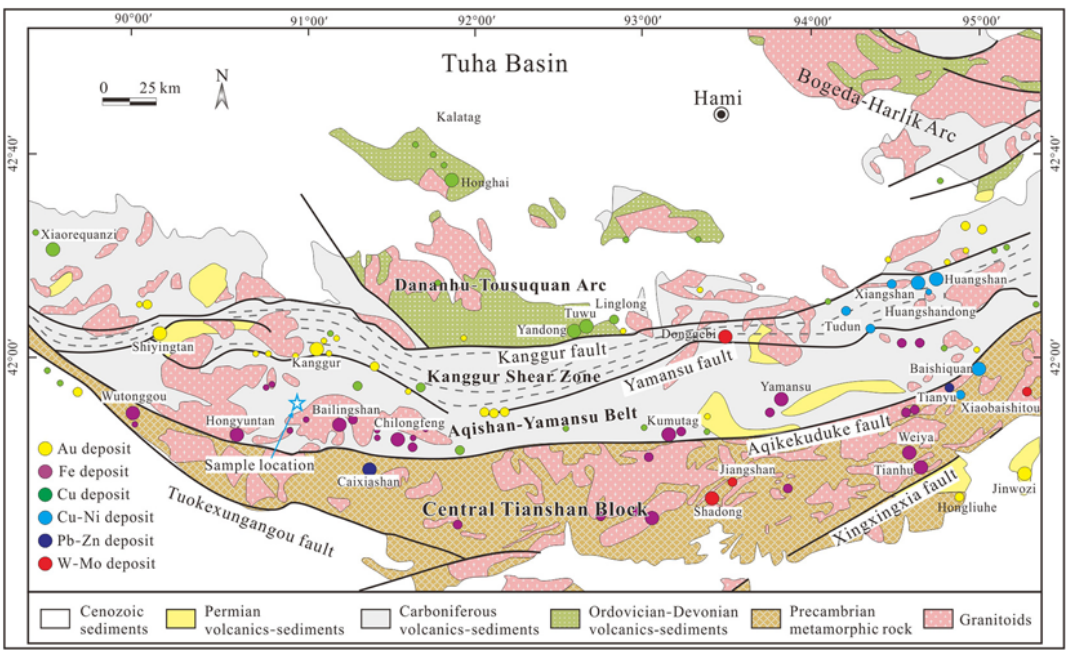

FIGURE 1 | Geologic map of the Chinese Eastern Tianshan Orogen (modified after Mao et al., 2005; Wang et al., 2006).

FIGURE 2 | Representative photographs showing the field relations, mineral assemblages and textural features for the dolerite: **(a)** Dolerite dyke cutting the Late Carboniferous volcaniclastic rocks. **(b)** Mafic rocks with medium- to fine-grained porphyritic texture. **(c)** Groundmasses of the dolerite with doleritic/interstitial texture. Abbreviations: Am = amphibole; Cpx = clinopyroxene; Ep = epidote; Pl = plagioclase.

orogenic Au and porphyry Mo deposits were formed at ca. 280 – 230 Ma (Zhang et al., 2015; Wang and Zhang, 2016; Wu et al., 2017).

The Aqishan-Yamansu belt comprises mainly Carboniferous intermediate-felsic volcanic-volcaniclastic rocks with minor marine sediment interbeds (Zhang et al., 2012; Han et al., 2019). These sequences are widely intruded by Carboniferous-Permian granitoids, which include the Bailingshan intrusive complex, Hongyuntan granodiorite and Xifengshan granite (Zhou et al., 2010; Zhang et al., 2016). Previous studies suggested that the widely-exposed felsic rocks are I-type and arc-related (Luo et al., 2016; Zhang et al., 2016; Zhao et al., 2019; Liu et al., 2020). The Aqishan-Yamansu island arc is well-known for hosting a series of Fe(-Cu) deposits, such as (from west to east) the Hongyuntan, Bailingshan, Yamansu, and Shaquanzi (Mao et al., 2005; Huang et al., 2013; Han et al., 2014; Hou et al., 2014; Jiang et al., 2018; Zhang et al., 2018a,b; Shi et al., 2021). The Central Tianshan Block is mainly consisted of a Precambrian metamorphic basement and Paleozoic active-margin magmatic sequences (Shu et al., 2002). Many skarn-type Fe and Pb-Zn deposits were formed during the Late Carboniferous (Zheng et al., 2015; Lu et al., 2018).

SAMPLING AND ANALYTICAL METHODS

Sampling

Dolerite dyke samples in this study were collected near the Bailingshan Fe deposit (41°48′07″N, 91°11′40″E) in the Aqishan-Yamansu belt, with a sampling interval of about 2 – 5 m from one dyke. In the field, the dolerite dyke (70 – 80 m long, 2 – 3 m wide) was observed to have intruded the Late Carboniferous volcaniclastic rocks (**Figure 2a**), suggesting a younger magmatic event.

TABLE 1 | Zircon U-Pb dating results for the study mafic dykes in the Eastern Tianshan.

Spot No.	Content (ppm)		Th/U	Isotopic ratios						Isotopic ages (Ma)					
	Th	U		$^{207}Pb/^{206}Pb$	1σ	$^{207}Pb/^{235}U$	1σ	$^{206}Pb/^{238}U$	1σ	$^{207}Pb/^{206}Pb$	1σ	$^{207}Pb/^{235}U$	1σ	$^{206}Pb/^{238}U$	1σ
βμ-01	1209	732	1.65	0.0543	0.0024	0.1562	0.0070	0.0209	0.0003	383	100	147	6	133	2
βμ-02	873	744	1.17	0.0535	0.0024	0.1513	0.0067	0.0206	0.0003	354	97	143	6	131	2
βμ-04	139	198	0.70	0.1221	0.0057	0.9643	0.0453	0.0568	0.0009	1987	88	686	23	356	6
βμ-06	132	162	0.82	0.0568	0.0030	0.4477	0.0233	0.0573	0.0011	483	117	376	16	359	7
βμ-07	576	487	1.18	0.0493	0.0033	0.1381	0.0095	0.0206	0.0006	165	157	131	8	132	4
βμ-08	474	350	1.36	0.0516	0.0056	0.1432	0.0165	0.0201	0.0004	333	49	136	15	128	2
βμ-09	143	243	0.59	0.0814	0.0057	0.4603	0.0310	0.0406	0.0006	1231	137	384	22	256	4
βμ-10	512	434	1.18	0.0484	0.0033	0.1350	0.0082	0.0206	0.0003	120	152	129	7	132	2
βμ-11	295	404	0.73	0.0543	0.0034	0.1563	0.0096	0.0209	0.0004	383	139	147	8	134	2
βμ-12	378	748	0.50	0.0615	0.0028	0.3260	0.0141	0.0384	0.0004	657	92	286	11	243	3
βμ-13	547	512	1.07	0.0484	0.0029	0.1355	0.0078	0.0204	0.0003	120	133	129	7	130	2
βμ-14	1735	1082	1.60	0.0526	0.0024	0.1457	0.0066	0.0201	0.0003	322	104	138	6	128	2
βμ-15	2205	1263	1.75	0.0505	0.0022	0.1387	0.0061	0.0197	0.0003	217	100	132	5	126	2
βμ-16	309	360	0.86	0.0558	0.0036	0.1541	0.0096	0.0200	0.0004	443	147	146	8	128	2
βμ-17	1640	1157	1.42	0.0527	0.0022	0.1473	0.0062	0.0202	0.0003	322	94	139	5	129	2
βμ-18	1551	1072	1.45	0.0523	0.0023	0.1448	0.0065	0.0199	0.0003	302	100	137	6	127	2
βμ-19	878	796	1.10	0.0490	0.0023	0.1363	0.0063	0.0200	0.0003	150	107	130	6	128	2
βμ-20	48.5	56.4	0.86	0.1127	0.0039	5.2078	0.1816	0.3344	0.0052	1844	58	1854	30	1860	25
βμ-21	686	519	1.32	0.0570	0.0032	0.1594	0.0087	0.0203	0.0004	500	126	150	8	130	2
βμ-22	473	580	0.82	0.0565	0.0021	0.4551	0.0164	0.0582	0.0008	472	83	381	11	365	5
βμ-23	1279	994	1.29	0.0560	0.0022	0.1631	0.0062	0.0212	0.0004	454	87	153	5	135	2
βμ-24	127	462	0.27	0.0856	0.0077	0.5544	0.0671	0.0416	0.0009	1329	174	448	44	263	6
βμ-25	323	314	1.03	0.0478	0.0037	0.1340	0.0094	0.0206	0.0004	100	161	128	8	132	2

The dolerite samples are dark green, and medium- to fine-grained porphyritic (**Figure 2b**). Euhedral plagioclase is the dominant phenocryst phase and commonly 1 to 3 mm long (**Figure 2b**). The doleritic-/interstitial-textured groundmass is composed mainly of subhedral plagioclase, clinopyroxene and trace Fe-Ti oxides (**Figure 2c**). Minor plagioclase and clinopyroxene grains in the samples are partially altered to epidote and amphibole, respectively. All the sample preparation and laboratory analyses were performed at the Wuhan SampleSolution Analytical Technology Co., Ltd. (WSATCL), China.

Zircon U-Pb Geochronology

After separated with the conventional density and magnetic separation techniques, zircon grains were hand-picked under a binocular microscope. The zircon internal structure was studied via cathodoluminescence (CL) imaging using an Analytical Scanning Electron Microscope (JSM − IT100).

Laser Ablation-Inductively Coupled Plasma-Mass Spectrometry (LA-ICP-MS) zircon U-Pb dating and trace element analysis for the dolerite samples were performed at the WSATCL. The laser ablation used 5 Hz frequency and 24 μm spot size. Each analysis comprises a background acquisition of approximately 20 - 30s, followed by 50s of sample data acquisition. The zircon 91500 and glass NIST610 were used as the external standard, and the Plešovice and GJ-1 zircons as the internal standard. Quantitative calibration for trace element analyses and U-Pb dating were conducted using ICPMSDataCal (Liu et al., 2008). Calculation of weighted mean ages and concordia diagram construction were performed using Isoplot/Ex 3.0 (Ludwig, 2003).

Whole-Rock Major and Trace Element Analyses

All the samples were first powdered to less than 200-mesh, then were placed in an oven at 105°C for drying of 12 h to determine LOI. The major element contents were measured by X-ray fluorescence (XRF) spectrometry (1 g powder for each sample), and the analytical precision is better than 1%. For trace elements (including REEs), 50 mg powder for each sample was dissolved in a mixture of 100ml HNO_3 and 100 ml HF. This solution was then analyzed with an Agilent 7700e ICP-MS, and the analytical precision is better than ± 5%.

Whole-Rock Sr-Nd Isotopes

Whole-rock Sr-Nd isotope analyses were conducted on a Neptune Plus Multi-Collector (MC)-ICP-MS, with the detailed analytical techniques as described by Wang et al. (2019). The $^{87}Rb/^{86}Sr$ and $^{147}Sm/^{144}Nd$ ratios were calculated using the Sr, Rb, Nd and Sm contents obtained by ICP-MS. All the measured Sr and Nd isotope ratios were

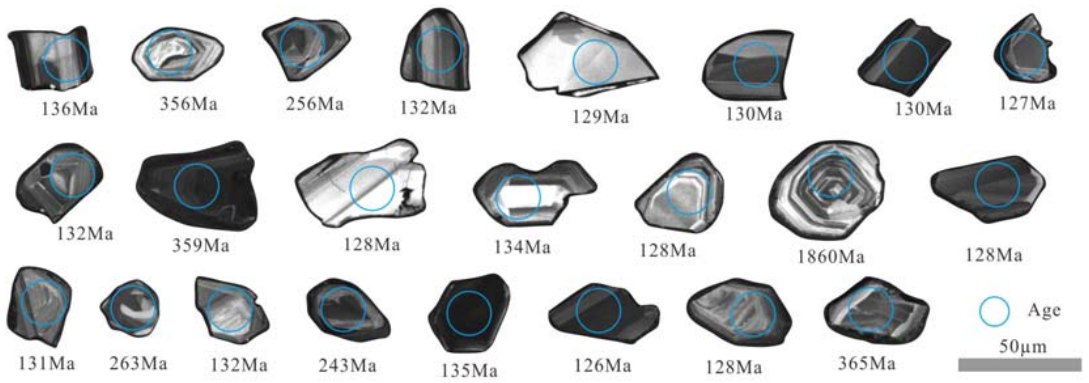

FIGURE 3 | Zircon CL images of the dolerite dyke.

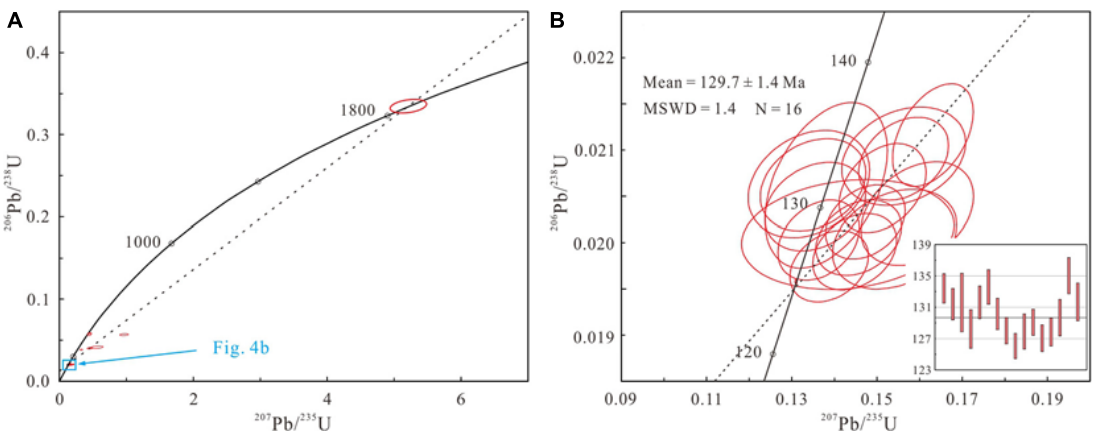

FIGURE 4 | (A) U-Pb concordia diagram of all the analytical zircon grains from the dolerite dyke. **(B)** U-Pb concordia diagram and weighted mean age of the concordant zircons.

normalized with $^{86}Sr/^{88}Sr$ = 0.1194 and $^{146}Nd/^{144}Nd$ = 0.7219, respectively (Lin et al., 2016). Analyses of the standards NIST SRM 987 and JNdi-1 during the measurement period yielded $^{87}Sr/^{86}Sr$ = 0.710244 ± 0.000022 (2σ) and $^{143}Nd/^{144}Nd$ = 0.512118 ± 0.000015 (2σ), similar to the recommended values (Tanaka et al., 2000).

RESULTS

Zircon U-Pb Ages

One sample was dated by zircon U-Pb analysis, and the results are given in **Table 1**. The zircons analyzed have wide ranges of U and Th contents, and all have high Th/U ratios (> 0.4). The zircon grains are transparent and euhedral-subhedral prismatic, indicating a magmatic origin (**Figure 3**; Belousova et al., 2002; Li, 2009). The 23 zircons analyzed show a wide $^{206}Pb/^{238}U$ age range (**Figure 4A**). The concordant zircons (n = 16) range from 136 to 126 Ma, yielding a weighted mean age of 129.7 ± 1.4 Ma (MSWD = 1.4; **Figure 4B**), which likely represents the dolerite crystallization age. Seven inherited/xenocrystic zircons were identified, including a Precambrian (1860 Ma), three Devonian-Carboniferous (365 to 356 Ma), and three Permian-Triassic (263 to 243 Ma) ones.

Whole-Rock Major and Trace Elements

Whole-rock major element and trace element contents of the dolerite dykes are listed in **Table 2**. As our samples are fresh or only slightly altered (e.g., weak epidote alteration in some plagioclase grains), the alteration effect on geochemistry is likely negligible. After normalized to 100 wt.% (anhydrous), the samples contain 49.4 to 50.1 wt.% SiO_2, 19.8 to 20.6 wt.% Al_2O_3, and 6.54 to 6.82 wt.% MgO. They have medium $Fe_2O_3^T$ content (8.43 to 8.71 wt.%) with corresponding Mg# (100*Mg/(Mg + Fe)) of 47 – 49. The rocks are sodic (Na_2O/K_2O = 4.71 to 6.80), and fall inside the basalt field in the TAS diagram (**Figure 5**; Wilson, 1989).

All the studied dolerite dykes display uniform chondrite-normalized REE patterns, as characterized by slight LREE enrichments ($(La/Yb)_N$ = 3.63 to 3.77) and subtle Eu anomalies

TABLE 2 | Major oxides (wt.%) and trace elements (ppm) abundances of the doleritic dykes in the Eastern Tianshan.

	β μ -01	β μ -02	β μ -03	β μ -04	β μ -05
Major oxides (wt.%)					
SiO_2	48.34	48.25	48.27	48.75	48.43
TiO_2	0.97	0.97	0.95	0.98	0.99
Al_2O_3	19.43	19.58	19.81	19.42	19.48
$Fe_2O_3^T$	8.44	8.45	8.16	8.52	8.44
FeO	4.90	4.42	4.60	4.38	4.42
MnO	0.13	0.15	0.14	0.13	0.13
MgO	6.60	6.41	6.43	6.39	6.36
CaO	9.68	9.54	9.56	9.87	9.78
Na_2O	2.69	2.75	2.72	2.76	2.76
K_2O	0.56	0.40	0.50	0.58	0.59
P_2O_5	0.25	0.26	0.25	0.26	0.25
Loss	2.52	2.66	2.65	2.39	2.43
Total	99.60	99.42	99.44	100.03	99.63
Trace elements (ppm)					
Sc	22.3	21.8	21.4	22.8	22.3
V	185	184	183	190	190
Cr	149	149	150	144	148
Co	35.6	36.0	35.9	37.1	36.8
Ni	121	113	116	113	112
Cu	75.3	64.4	47.0	72.1	82.3
Zn	57.7	65.9	56.2	57.4	57.7
Ga	17.7	18.2	18.0	18.5	18.2
Rb	19.8	13.5	18.2	25.5	25.3
Sr	541	524	535	552	544
Y	19.4	20.4	19.7	20.6	20.1
Zr	104	99	99	107	106
Nb	4.40	4.31	4.22	4.50	4.52
Cs	0.96	0.84	0.69	1.48	1.42
Ba	153	106	115	158	142
La	9.25	9.20	9.05	9.70	9.48
Ce	22.4	23.0	22.6	24.2	23.4
Pr	3.06	3.07	3.04	3.24	3.17
Nd	13.9	14.0	13.6	14.7	14.2
Sm	3.79	3.73	3.67	3.78	3.74
Eu	1.12	1.20	1.16	1.19	1.18
Gd	3.51	3.48	3.62	3.66	3.56
Tb	0.55	0.56	0.54	0.56	0.55
Dy	3.47	3.44	3.35	3.78	3.54
Ho	0.72	0.69	0.71	0.72	0.72
Er	1.90	1.92	1.86	2.00	1.99
Tm	0.29	0.28	0.27	0.30	0.30
Yb	1.77	1.82	1.75	1.88	1.80
Lu	0.27	0.27	0.26	0.28	0.28
Hf	2.39	2.21	2.35	2.37	2.40
Ta	0.27	0.28	0.26	0.29	0.28
Pb	3.49	3.33	3.30	3.66	3.70
Th	0.66	0.63	0.63	0.65	0.65
U	0.26	0.23	0.24	0.25	0.25
Na_2O/K_2O	4.82	6.80	5.42	4.80	4.71
Mg#	49	48	49	49	47
Nb/U	16.7	18.5	17.9	17.9	18.1
Ce/Pb	6.43	6.90	6.85	6.61	6.33
Sm/Yb	2.14	2.05	2.09	2.01	2.08
Dy/Yb	1.96	1.89	1.91	2.01	1.97
$(La/Yb)_N$	3.75	3.63	3.70	3.70	3.77
Eu/Eu*	0.93	1.01	0.96	0.97	0.97

(Eu/Eu* = 0.93 to 1.01) (**Figure 6A**). In the primitive mantle-normalized multi-element plot (**Figure 6B**), the samples are enriched in large-ion lithophile element (LILE; e.g., Rb, K, Sr, and Pb) and depleted in HFSEs.

Whole-Rock Sr-Nd Isotopes

Whole-rock Sr-Nd isotope compositions of the studied samples are presented in **Table 3**. Initial isotope ratios were back-calculated to the dolerite crystallization age of 130 Ma. The samples have low initial $^{87}Sr/^{86}Sr$ (0.7041 to 0.7043) and positive $\varepsilon_{Nd}(t)$ (+ 4.6 to + 5.1) values, yielding depleted mantle Nd one-stage model ages (T_{DM1}) of 746 – 882 Ma. In the $(^{87}Sr/^{86}Sr)_i$ vs. $(^{143}Nd/^{144}Nd)_i$ diagram (**Figure 7**), all samples plot in the ocean island basalt (OIB) field (Hart, 1985), similar to the Permian Huangshanxi gabbro in the Eastern Tianshan (Zhang et al., 2011; Deng et al., 2015).

DISCUSSION

Fractional Crystallization and Crustal Contamination

The dolerite samples have much lower Mg# (47 – 49), Cr (144 – 150 ppm) and Ni (112 – 121 ppm) contents (**Table 2**) than typical mantle-derived melts (Mg# = 71 – 83, Cr > 1000 ppm and Ni > 400 ppm; Wilson, 1989; Wang et al., 2019), suggesting that their parental magma may have experienced fractional crystallization. Rayleigh fractional crystallization model calculations were conducted to determine the fractionation phase (Wilson, 1989), which shows that all samples plot between the olivine and pyroxene evolution trends in the Cr-Ni diagram (**Figure 8A**). This indicates significant fractionation of olivine and pyroxene. Fractionation of Ti-bearing minerals (e.g., spinel) in the dolerite is evidenced by the negative Nb, Ta and Ti anomalies and the Nb-Ta fractional crystallization model diagram (**Figure 8B**; Saunders et al., 1992; Hawkesworth et al., 1993). The lack of negative Sr and Eu anomalies in the samples suggests limited plagioclase fractionation (**Figure 6**).

Mantle-derived magmas commonly assimilate crustal components during their ascent, which altered their geochemical characteristics (e.g., LREE and LILE enrichments and HFSE depletions; Wilson, 1989; Rudnick and Gao, 2014), as found also in the dolerite dykes (**Figure 6**). This clearly suggests certain degrees of crustal contamination for the doleritic magma. Element pairs (e.g., Nb and U, Ce, and Pb) with similar bulk-solid/melt partition coefficients cannot be significantly

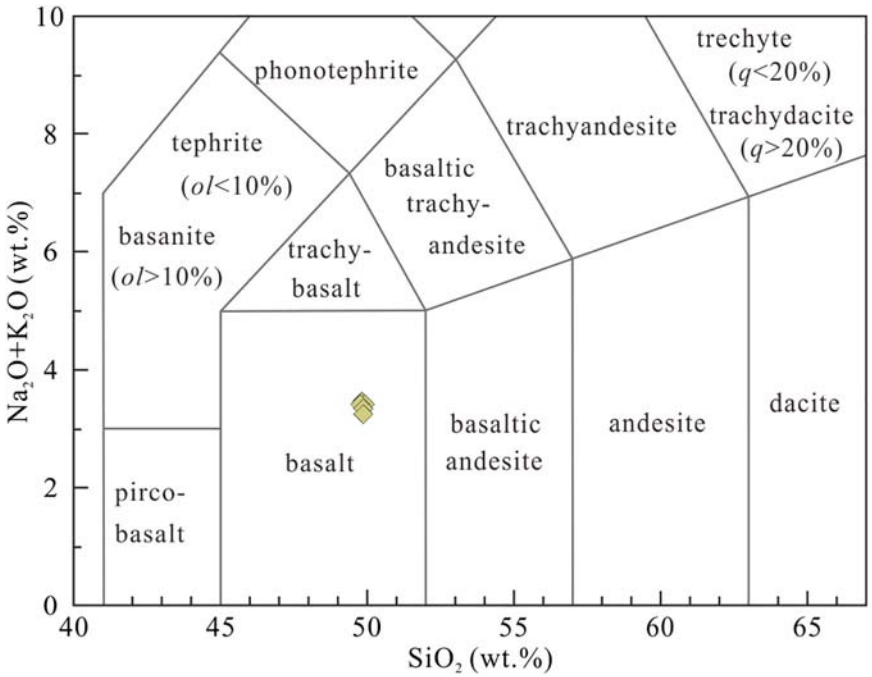

FIGURE 5 | K_2O vs. SiO_2 diagram for the samples (after Peccerillo and Taylor, 1976).

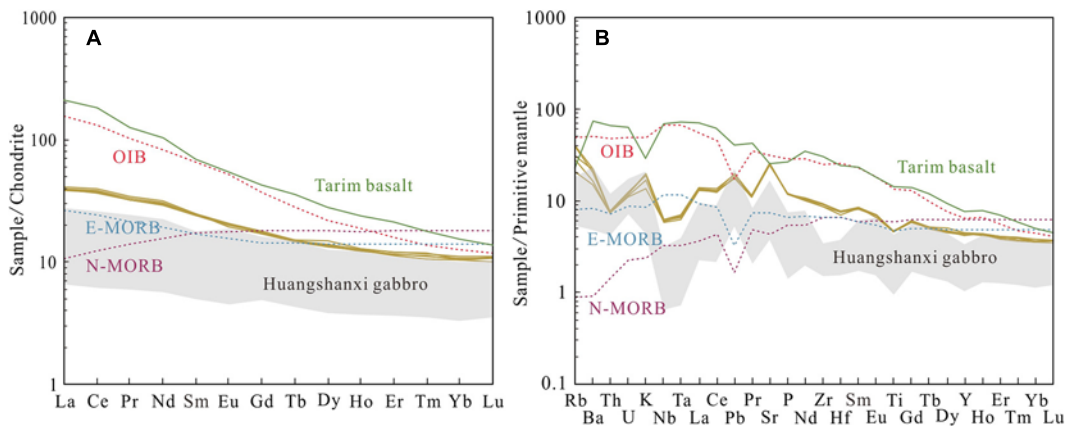

FIGURE 6 | (A) Chondrite-normalized REE patterns; **(B)** Primitive mantle-normalized multi-element diagrams. Data of average primitive mantle, E-MORB, N-MORB and OIB are from Sun and McDonough (1989). Compositions of chondrite, Tarim basalts and Huangshanxi gabbro are from Boynton (1984); Zhou et al. (2009) and Zhang et al. (2011), respectively.

TABLE 3 | Sr and Nd isotopic compositions of doleritic samples from the Eastern Tianshan.

	Rb (ppm)	Sr (ppm)	$^{87}Rb/^{86}Sr$	$^{87}Sr/^{86}Sr$	2σ	$(^{87}Sr/^{86}Sr)_i$	Sm (ppm)	Nd (ppm)	$^{147}Sm/^{144}Nd$	$^{143}Nd/^{144}Nd$	2σ	$(^{143}Nd/^{144}Nd)_i$	$\varepsilon_{Nd}(t)$	TDM_1 (Ga)
βμ-01	19.8	541	0.105745	0.704445	0.0000086	0.7043	3.79	13.9	0.164782	0.512867	0.0000056	0.5127	5.0	0.88
βμ-02	13.5	524	0.074352	0.704215	0.0000085	0.7041	3.73	14.0	0.161012	0.512865	0.0000064	0.5127	5.0	0.82
βμ-03	18.2	535	0.098366	0.704239	0.0000085	0.7041	3.67	13.6	0.162885	0.512872	0.0000078	0.5127	5.1	0.83
βμ-04	25.5	552	0.133849	0.704579	0.0000109	0.7043	3.78	14.7	0.154996	0.512863	0.0000065	0.5127	5.1	0.75
βμ-05	25.3	544	0.134156	0.704471	0.0000116	0.7042	3.74	14.2	0.159375	0.512842	0.0000126	0.5127	4.6	0.86

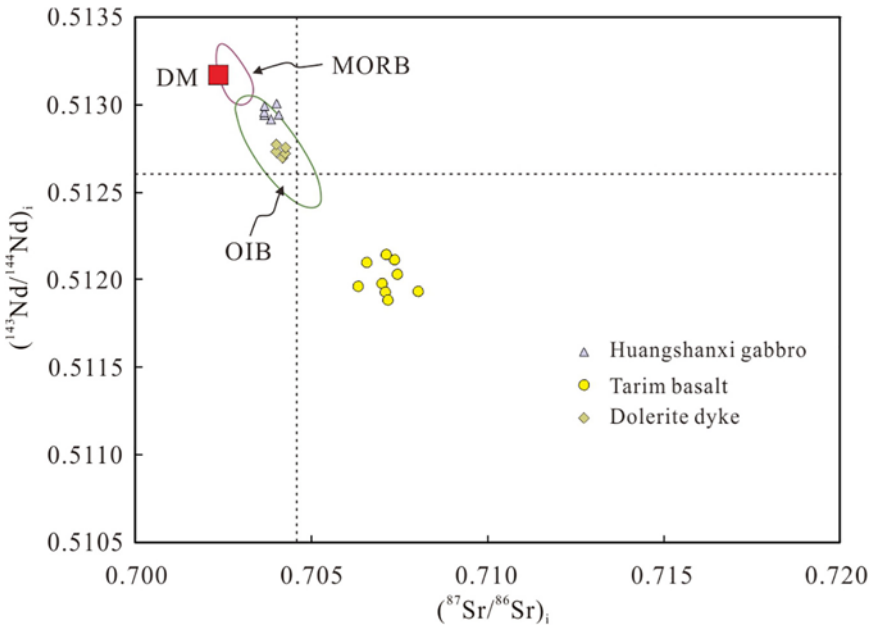

FIGURE 7 | $\varepsilon_{Nd}(t)$ vs. I_{Sr} diagram for the dolerite dyke. All data were calculated to the corresponding zircon U-Pb ages. Data source: Tarim basalts (Zhou et al., 2009); Huangshanxi gabbro (Zhang et al., 2011); DM (Salters and Stracke, 2004). The OIB and MORB fields are after Hart (1985) and Wilson (1989), respectively.

segregated through partial melting or fractional crystallization, and their ratios remain roughly constant and reflect those of the magma source (Hofmann, 1997). The dolerite samples have Nb/U (16.7 to 18.5) and Ce/Pb (6.33 to 6.90) values intermediate between the mantle array (OIB/MORB) and continental crust, also suggesting crustal assimilation (**Figure 9**). Crustal contamination is also evidenced by the presence of xenocrystic zircons in the samples (**Figure 4A**). To summary, both fractional crystallization and crustal contamination occurred during the Cretaceous magma emplacement at/around Bailingshan.

Magma Source

Mafic magmas can be derived from the lithospheric or asthenospheric mantle (Wilson, 1989; Shellnutt, 2014). The lithospheric mantle is generally cooler and isotopically more-enriched due to its interactions with subduction-derived melts and/or fluids and its long isolation from the mantle convection underneath. In contrast, asthenospheric mantle is commonly hotter and isotopically more-depleted (Saunders et al., 1992; Hofmann, 1997). Our dolerite samples have low initial $^{87}Sr/^{86}Sr$ (0.7041 to 0.7043) and positive $\varepsilon_{Nd}(t)$ (+ 4.6 to + 5.1) values, plotting near the MORB field and overlap with typical OIB (**Figure 7**), which suggests an asthenospheric mantle source. This conclusion agrees with published work on the Huangshanxi gabbro, which also pointed to a depleted asthenospheric mantle source beneath the Eastern Tianshan Orogen (Zhang et al., 2011; Deng et al., 2015). As above-discussed, the slight LREE enrichments and distinct negative Nb, Ta and Ti anomalies of the dolerite samples were likely caused by fractional crystallization and crustal assimilation during the magma emplacement.

Since garnet has high partition coefficients for Yb ($D_{garnet/melt}$ = 6.6) relative to Sm ($D_{garnet/melt}$ = 0.25), low-degree partial melting of mantle lherzolite (with garnet residue) would strongly increase the Sm/Yb ratios (Green, 2006; Jung et al., 2006). In contrast, partial melting of mantle spinel lherzolite does not markedly change the Sm/Yb ratios, since spinel has similar partition coefficients for Sm and Yb (McKenzie and O'Nions, 1991; Kelemen et al., 1993). Therefore, mafic magma source can be effectively constrained by fractionation of Sm and Yb (Ellam, 1992; Aldanmaz et al., 2000; Zhang et al., 2015). Our dolerite dykes have slightly elevated Sm/Yb ratios (2.01 to 2.14), and all samples plot near the spinel-garnet lherzolite model curve in the partial melting model diagram (**Figure 10**). This suggests that the parental magma was likely generated by low-degree partial melting of a spinel-garnet lherzolite mantle source at 70 – 80 km depth, which is where the spinel-to-garnet transition is located (McKenzie and O'Nions, 1991).

Tectonic Implications

As discussed above, the dolerite dykes were mainly generated by low-degree partial melting of the asthenospheric mantle. Mafic rocks of similar petrogenesis were proposed to have formed in tectonic events including subducting slab break-off (Davies and von Blanckenburg, 1995; Deng et al., 2015; Zhang et al., 2015), mantle plume upwelling (Campbell and Griffiths, 1990; Bryan and Ernst, 2008; Zhou et al., 2009), continental rifting (Corti, 2009; Thybo and Nielsen, 2009), and lithospheric delamination (Hoernle et al., 2006; McGee and Smith, 2016; Wang et al., 2019).

Slab break-off usually occurs during incipient continent-continent collision (Davies and von Blanckenburg, 1995).

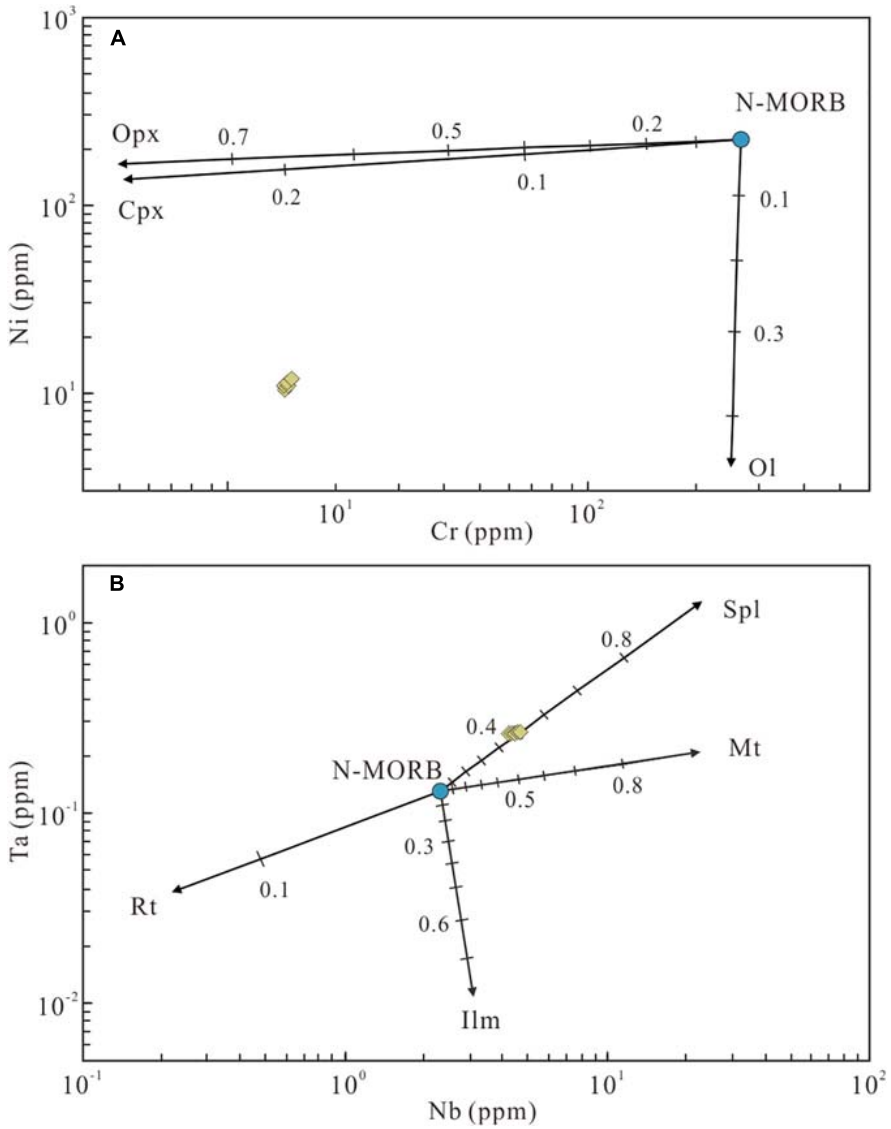

FIGURE 8 | Rayleigh fractionation modal calculations for trace elements **(A)** Cr-Ni, **(B)** Nb-Ta. Partition coefficients (KD) are from http://earthref.org/GERM/, and N-MORB compositions are from Sun and McDonough (1989). Abbreviations: Cpx = clinopyroxene; Ilm = ilmenite; Mt = magnetite; Ol = olivine; Opx = orthopyroxene; Pl = plagioclase; Rt = rutile; Spl = spinel.

Under this setting, the hot asthenospheric mantle would rise through the slab window, and partially melted the overlying metasomatized lithosphere (Rogers et al., 2002; Bonin, 2004; Ferrari, 2004). Therefore, the resulting magmatism would be focused along linear trends (Davies and von Blanckenburg, 1995). In/around our study area, no coeval linear magmatic trends are observed or ever reported, inconsistent with a slab break-off model. Considering the regional tectonic evolution, it is widely considered that the Eastern Tianshan was in a post-collisional setting since the Triassic (Wu et al., 2006; Zhang et al., 2015; Zhao et al., 2019), after the Kanggur Ocean closure and the subsequent Junggar-Central Tianshan collision (Xiao et al., 2008; Wang et al., 2014; Zhang et al., 2016; Zhao et al., 2019). Hence, we suggested that the Cretaceous dolerite was unlikely produced by slab break-off. The dolerite samples display obvious negative Nb, Ta and Ti anomalies, significantly different from typical OIB-like, mantle plume-related Tarim flood basalts (Zhou et al., 2009). The small volume of Cretaceous Eastern Tianshan mafic rocks is also inconsistent with a large igneous province (LIP) origin (Campbell and Griffiths, 1990; Bryan and Ernst, 2008). Furthermore, no geophysical evidence is available to show the presence of mantle plume beneath the Eastern Tianshan. Hence, we considered that the dolerite was unlikely to be mantle plume-related. The continental rift model involves narrow and long tectonic depressions in the lithosphere, leading to partial melting of the upwelling asthenospheric mantle (Corti, 2009; Thybo and Nielsen, 2009).

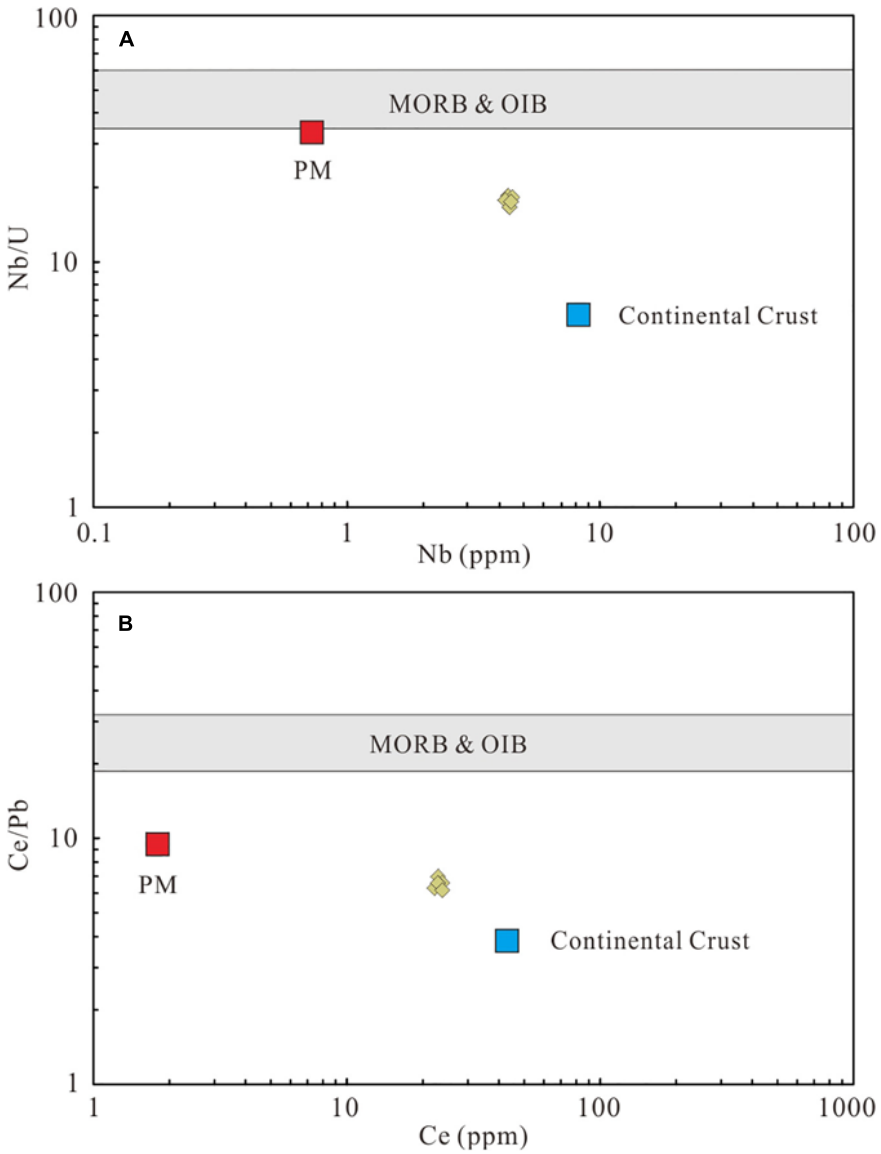

FIGURE 9 | (A) Nb/U vs. Nb; **(B)** Ce/Pb vs. Ce diagrams for the dolerite dyke. Average ratios of Nb/U and Ce/Pb in OIB and MORB are after Hofmann (1997), and data for primitive mantle (Sun and McDonough, 1989) and average continental crust (Rudnick and Gao, 2014) are also shown for comparison.

Key features of this model include an elongated topographic trough and Moho shallowing (Thybo and Nielsen, 2009). However, graben structures are absent in the Eastern Tianshan, suggesting that a continental rift scenario was unlikely either.

Decompression through lithospheric delamination, accompanied by crustal extension, is another possible mechanism to explain the melting of upwelling asthenosphere (Marotta et al., 1998; McGee and Smith, 2016). Jull and Kelemen (2001) reported that the subduction-modified lower lithospheric mantle is denser than the normal upper lithospheric mantle. This makes the lower lithospheric mantle to sink into the underlying asthenosphere, and the latter rises up to take its place (Kay and Kay, 1993; Xu et al., 2002). In the Eastern Tianshan, many recent works documented that Carboniferous arc-related igneous rocks were extensively developed due to the subduction of Kanggur ocean basin (Xiao et al., 2008; Wang et al., 2014; Luo et al., 2016; Zhang et al., 2016; Zhao et al., 2019). This process has likely added oceanic materials into the deep lithospheric mantle beneath the Eastern Tianshan. After that, the high-density lithospheric root was probably removed, resulting in asthenospheric mantle upwelling and the Bailingshan dolerite dyke emplacement. This suggestion is supported by the intraplate tectonic classification in the Zr vs. Zr/Y diagram (**Figure 11**). Zhao et al. (2019) suggested that the Triassic (ca. 235 Ma) felsic magmatism was derived from partial melting of thickened juvenile lower crust, and Zhang et al. (2017) reported that the Duotoushan adakitic dacite porphyry was emplaced via delamination process at around 197 Ma. These

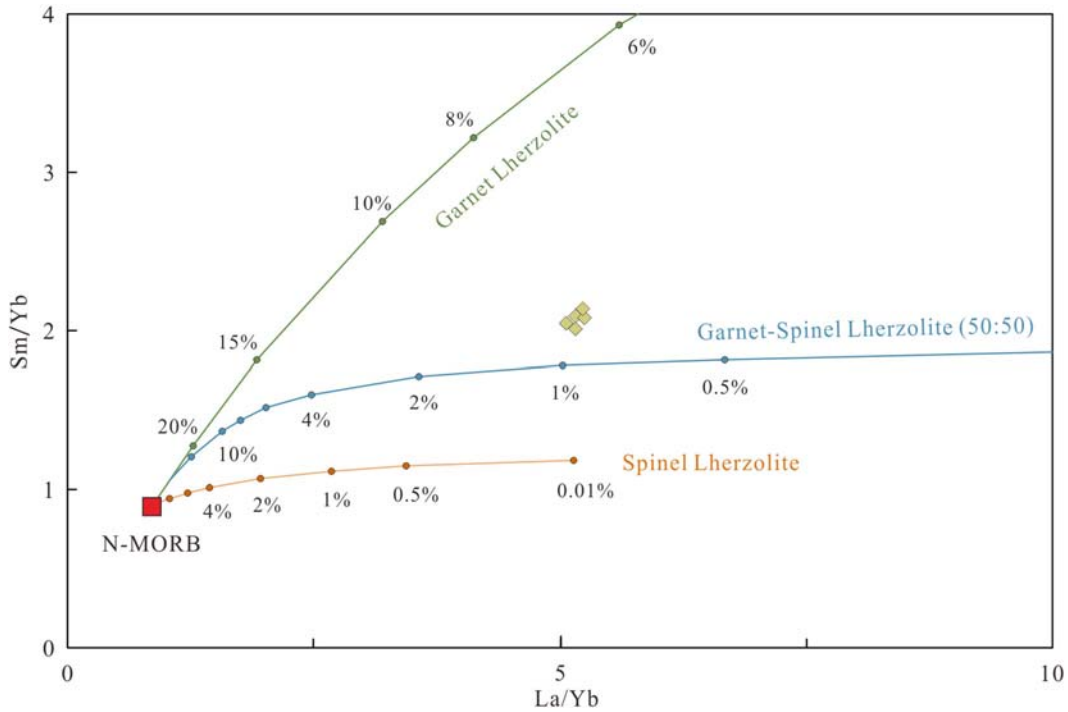

FIGURE 10 | Plots of Sm/Yb vs. La/Yb, showing melting curves obtained with the batch melting equation: $C_1/C_0 = 1/[D + F(1-P)]$ (after Wilson, 1989). C_1: Concentration of a trace element in the melt; C_0: Concentration of the same element in original un-melted source; D: Bulk partition coefficient of the source; P: Proportion of phase entering the melt; F: Melt fraction. Reference curves are the melting trends of spinel lherzolite, garnet lherzolite, and spinel-garnet (50:50) lherzolite. Initial compositions of N-MORB are from Sun and McDonough (1989). Assumed weight fractions of Ol, Opx, Cpx, and Sp in the spinel lherzolite are 0.578, 0.270, 0.119, and 0.033, respectively. Proportions of Ol, Opx, Cpx, and Spl entering the melt are 0.100, 0.270, 0.500, and 0.130, respectively. For garnet lherzolite, the weight fractions of Ol, Opx, Cpx, and Grt in the mineral assemblage are 0.598, 0.211, 0.076, and 0.115, respectively, with melt mode of 0.050, 0.200, 0.300, and 0.450, respectively. Abbreviations: Cpx = clinopyroxene; Grt = garnet; Ol = olivine; Opx = orthopyroxene; Spl = spinel.

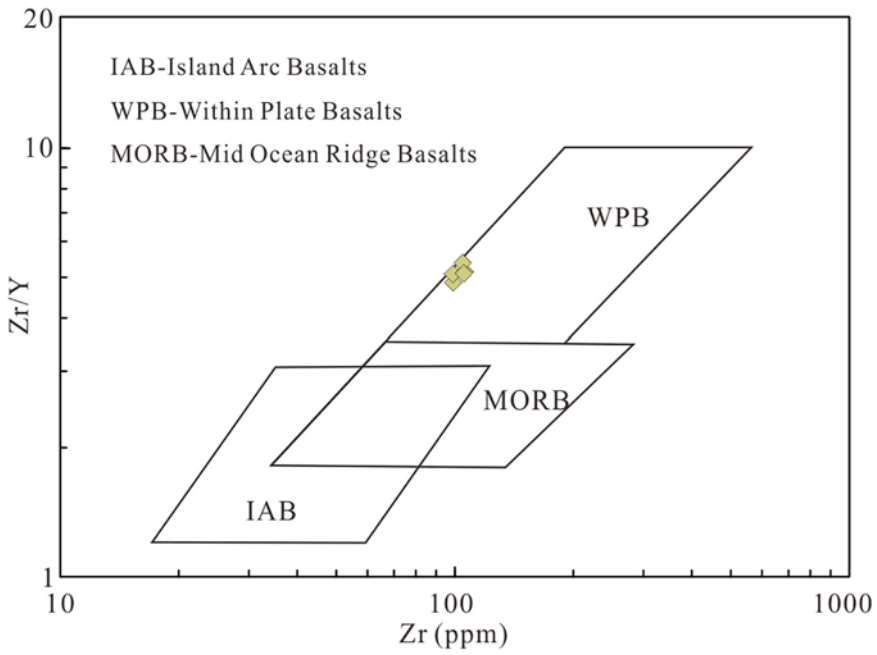

FIGURE 11 | Zr vs. Zr/Y diagram for the dolerite dyke (modified after Pearce and Norry, 1979).

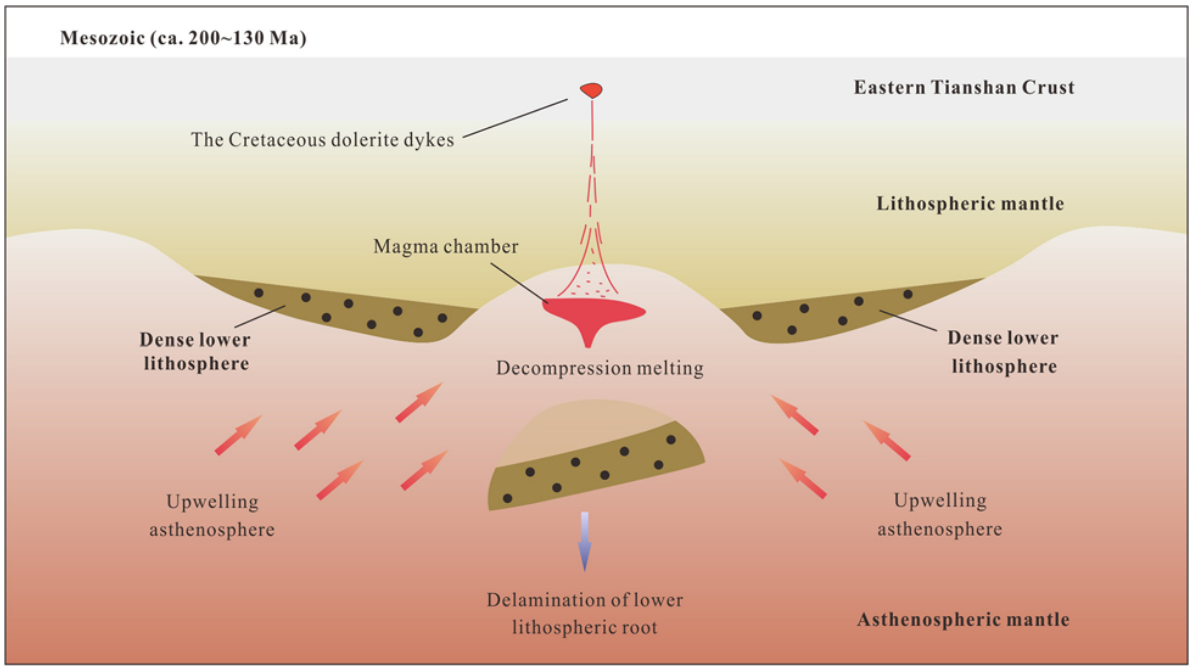

FIGURE 12 | Lithospheric delamination model and the formation of Cretaceous Eastern Tianshan intraplate magmatism (after Wang et al., 2019).

observations indicate an Early Jurassic tectonic transition from post-collisional to intraplate setting in the Eastern Tianshan. Together with our new newly data, we proposed that the removal of the high-density lithospheric root may have continued to the Cretaceous.

To summarize, we have constructed a modified tectonic model to explain the Cretaceous intraplate magmatism in the Eastern Tianshan (**Figure 12**). In our model, the lower lithospheric mantle was modified by oceanic crustal input from the Late Paleozoic subduction, which increased its density. The density imbalance with the less-dense asthenospheric mantle beneath may have caused a small-scale lithospheric root removal. Consequently, the asthenospheric mantle upwelled and partially melted, and formed the parental melt of the Bailingshan dolerite dykes.

CONCLUSION

(1) Zircon U-Pb dating of the Bailingshan dolerite dykes from the Eastern Tianshan yielded an Early Cretaceous age (129.7 ± 1.4 Ma).
(2) Parental magma of the dolerite dykes was likely derived from low-degree partial melting of the asthenospheric mantle in the spinel-garnet stability field, and undergone fractionation and crustal assimilation during its ascent.
(3) Formation of the Cretaceous Eastern Tianshan dolerite dykes was likely in an intraplate extension setting, and related to the sinking of dense, subduction-modified lower lithospheric mantle.

DATA AVAILABILITY STATEMENT

The original contributions presented in the study are included in the article/supplementary material, further inquiries can be directed to the corresponding author/s.

AUTHOR CONTRIBUTIONS

WZ and XD conceived this research. WZ wrotes the manuscript and prepares the figures. BT, LP, and XJ reviews and supervises the manuscript. The co-authors XD are involved in the discussion of the manuscript. All authors finally approved the manuscript and thus agreed to be accountable for this work.

FUNDING

This study was funded by the National Natural Science Foundation of China (41702099) and the China Geological Survey (DD20190050, DD20201121).

ACKNOWLEDGMENTS

We thank Hongfang Chen for helping with the LA-MC-IC-PMS zircon analysis, and Run Zhou and Xianshen Yu for helping with the field work. Special thanks are also due to Editor-in-Chief Prof. David Lentz and Guest Editor Dr. Chun-Kit Lai, as well as two reviewers for their constructive comments and insightful reviews, which significantly enhanced the manuscript.

REFERENCES

Aldanmaz, E., Pearce, J. A., Thirlwall, M. F., and Mitchell, J. G. (2000). Petrogenetic evolution of late Cenozoic, post-collision volcanism in western Anatolia, Turkey. *J. Volcanol. Geotherm. Res.* 102, 67–95. doi: 10.1016/s0377-0273(00)00182-7

Belousova, E., Griffin, W. L., O'Reilly, S. Y., and Fisher, N. L. (2002). Igneous zircon: trace element composition as an indicator of source rock type. *Contrib. Mineral. Petrol.* 143, 602–622. doi: 10.1007/s00410-002-0364-7

Bonin, B. (2004). Do coeval mafic and felsic magmas in post-collisional to within-plate regimes necessarily imply two contrasting, mantle and crustal, sources? A review. *Lithos* 78, 1–24. doi: 10.1016/j.lithos.2004.04.042

Boynton, W. V. (1984). "Geochemistry of the rare earth elements: meteorite studies," in *Rare Earth Element Geochemistry*, ed. P. Henderson (Amsterdam: Elsevier), 63–114. doi: 10.1016/b978-0-444-42148-7.50008-3

Bryan, S. E., and Ernst, R. E. (2008). Revised definition of large igneous provinces (LIPs). *Earth Sci. Rev.* 86, 175–202. doi: 10.1016/j.earscirev.2007.08.008

Campbell, I. H., and Griffiths, R. W. (1990). Implications of mantle plume structure for the evolution of flood basalts. *Earth Planet. Sci. Lett.* 99, 79–93. doi: 10.1016/0012-821x(90)90072-6

Chen, B., and Jahn, B. M. (2004). Genesis of post-collisional granitoids and basement nature of the Junggar Terrane, NW China: Nd-Sr isotope and trace element evidence. *J. Asian Earth Sci.* 23, 691–703. doi: 10.1016/s1367-9120(03)00118-4

Corti, C. (2009). Continental rift evolution: from rift initiation to incipient break-up in the Main Ethiopian Rift, East Africa. *Earth Sci. Rev.* 96, 1–53. doi: 10.1016/j.earscirev.2009.06.005

Davies, J. H., and von Blanckenburg, F. (1995). Slab breakoff: a model of lithospheric detachment and its test in the magmatism and deformation of collisional orogens. *Earth Planet. Sci. Lett.* 129, 85–102. doi: 10.1016/0012-821x(94)00237-s

Deng, Y. F., Song, X. Y., Hollings, P., Zhou, T. F., Yuan, F., Chen, L. M., et al. (2015). Role of asthenosphere and lithosphere in the genesis of the Early Permian Huangshan mafic–ultramafic intrusion in the Northern Tianshan, NW China. *Lithos* 227, 241–254. doi: 10.1016/j.lithos.2015.04.014

Ellam, R. M. (1992). Lithospheric thickness as a control on basalt geochemistry. *Geol.* 20, 153–156. doi: 10.1130/0091-7613(1992)020<0153:ltaaco>2.3.co;2

Ferrari, L. (2004). Slab detachment control on mafic volcanic pulse and mantle heterogeneity in central Mexico. *Geol.* 32, 77–80. doi: 10.1130/g19887.1

Green, N. L. (2006). Influence of slab thermal structure on basalt source regions and melting conditions: REE and HFSE constraints form the Garibaldi volcanic belt, northern Cascadia subduction system. *Lithos.* 87, 23–49. doi: 10.1016/j.lithos.2005.05.003

Han, C. M., Xiao, W. J., Zhao, G. C., Ao, S., Zhang, J., Qu, W., et al. (2010). In-situ U-Pb, Hf and Re-Os isotopic analyses of the Xiangshan Ni-Cu-Co deposit in Eastern Tianshan (Xinjiang), Central Asia Orogenic Belt: constraints on the timing and genesis of the mineralization. *Lithos* 120, 547–562. doi: 10.1016/j.lithos.2010.09.019

Han, C. M., Xiao, W. J., Zhao, G. C., Su, B. X., Sakyi, P. A., Ao, S., et al. (2014). Late Paleozoic metallogenesis and evolution of the east tianshan orogenic belt (NW China, Central Asia Orogenic Belt). *Geol. Ore Deps.* 56, 493–512. doi: 10.1134/s1075701514060075

Han, J. S., Chen, H. Y., Jiang, H. J., Zhao, L. D., Zhang, W. F., and Lai, C. K. (2019). Genesis of the Paleozoic Aqishan-Yamansu arc-basin system and Fe (-Cu) mineralization in the Eastern Tianshan, NW China. *Ore Geol. Rev.* 105, 55–70. doi: 10.1016/j.oregeorev.2018.12.012

Hart, W. K. (1985). Chemical and isotopic evidence for mixing between depleted and enriched mantle, northwestern U.S.A. *Geochim. Cosmochim. Acta.* 49, 131–144. doi: 10.1016/0016-7037(85)90197-8

Hawkesworth, C. J., Gallagher, K., Hergt, J. M., and McDermott, F. (1993). Mantle and Slab contributions in ARC Magmas. *Annu. Rev. Earth Planet. Sci.* 21, 175–204. doi: 10.1146/annurev.ea.21.050193.001135

Hoernle, K., White, J. D. L., Bogaard, P. V. D., Hauff, F., Coombs, D. S., Werner, R., et al. (2006). Cenozoic intraplate volcanism on New Zealand: upwelling induced by lithospheric removal. *Earth Planet. Sci. Lett.* 248, 350–367. doi: 10.1016/j.epsl.2006.06.001

Hofmann, A. W. (1997). Mantle geochemistry: the message from oceanic volcanism. *Nature* 385, 219–229. doi: 10.1038/385219a0

Hou, T., Zhang, Z. C., Santosh, M., Encarnacion, J., Zhu, J., and Luo, W. Q. (2014). Geochronology and geochemistry of submarine volcanic rocks in the Yamansu iron deposit, Eastern Tianshan Mountains, NW China: constraints on the metallogenesis. *Ore Geol. Rev.* 56, 487–502. doi: 10.1016/j.oregeorev.2013.03.008

Huang, X. W., Qi, L., Gao, J. F., and Zhou, M. F. (2013). First reliable Re-Os ages of pyrite and stable Isotope Compositions of Fe (-Cu) deposits in the hami region, eastern tianshan Orogenic Belt, NW China. *Resour. Geol.* 63, 166–187. doi: 10.1111/rge.12003

Ishizuka, O., Tani, K., and Reagan, M. K. (2014). Izu-bonin-mariana forearc crust as a modern ophiolite analogue. *Elements* 10, 115–120. doi: 10.2113/gselements.10.2.115

Jiang, H. J., Han, J. S., Chen, H. Y., Zheng, Y., Zhang, W. F., Lu, W. J., et al. (2018). Hydrothermal alteration, fluid inclusions and stable isotope characteristics of the Shaquanzi Fe–Cu deposit, Eastern Tianshan: implications for deposit type and metallogenesis. *Ore Geol. Rev.* 100, 385–400. doi: 10.1016/j.oregeorev.2016.09.025

Jull, M., and Kelemen, P. B. (2001). On the conditions for lower crustal convective instability. *J. Geophys. Res.* 106, 6423–6446. doi: 10.1029/2000jb900357

Jung, C., Jung, S., Hoffer, E., and Berndt, J. (2006). Petrogenesis of tertiary mafic alkaline magmas in the hocheifel. *Germany. J. Petrol.* 47, 1637–1671. doi: 10.1093/petrology/egl023

Kay, R. W., and Kay, S. M. (1993). Delamination and delamination magmatism. *Tectonophysics* 219, 177–189. doi: 10.1016/0040-1951(93)90295-u

Kelemen, P. B., Shimizu, N., and Dunn, T. (1993). Relative depletion of niobium in some arc magmas and the continental crust: partitioning of K, Nb, La, and Ce during melt/rock reaction in the upper mantle. *Earth Planet. Sci. Lett.* 120, 111–134. doi: 10.1016/0012-821x(93)90234-z

Li, C. M. (2009). A Review on the minerageny and situ microanalytical dating techniques of zircons. *Geol. Surv. Res.* 33, 161–174.

Li, D. D., Wang, Y. W., Shi, Y., Xie, H. J., Wang, J. B., and Lai, C. (2019). Age and geochemistry of the Carboniferous-Permian magmatism and Fe-Ti-V oxide metallogeny in the Eastern Tianshan Orogen, NW China: evidence from the Yaxi mafic-ultramafic complex. *Int. Geol. Rev.* 61, 853–867. doi: 10.1080/00206814.2018.1474499

Li, J. Y., Wang, K. Z., Sun, G. H., Mo, S. G., Li, W. Q., Yang, T. N., et al. (2006). Paleozoic active margin slices in the southern Turfan-Hami basin: geological records of subduction of the Paleo-Asian ocean plate in Central Asian regions. *Acta Petrol. Sin.* 22, 1087–1102.

Lin, J., Liu, Y. S., Yang, Y. H., and Hu, Z. C. (2016). Calibration and correction of LA-ICP-MS and LA-MC-ICP-MS analyses for element contents and isotopic ratios. *Solid Earth Sci.* 1, 5–27. doi: 10.1016/j.sesci.2016.04.002

Liu, B., Wu, J. H., Li, H., Mathur, R., Wu, Q. H., Zheng, H., et al. (2020). Late Paleozoic tectonic evolution of the Kangguer Shear Zone and Yamansu Arc Belt, Eastern Tianshan (NW China): constraints from structure, petrogenesis and geochronology of granitoids. *Lithos* 380–381:105821. doi: 10.1016/j.lithos.2020.105821

Liu, Y. S., Hu, Z. C., Gao, S., Günther, D., Xu, J., Gao, C. G., et al. (2008). In-situ analysis of major and trace elements of anhydrous minerals by LA-ICP-MS without applying an internal standard. *Chem. Geol.* 257, 34–43. doi: 10.1016/j.chemgeo.2008.08.004

Lu, W. J., Zhang, L., Chen, H. Y., Han, J. S., Jiang, H. J., Li, D. F., et al. (2018). Geology, fluid inclusion and isotope geochemistry of the Hongyuan reworked sediment-hosted Zn–Pb deposit: metallogenic implications for Zn–Pb deposits in the Eastern Tianshan, NW China. *Ore Geol. Rev.* 100, 504–533. doi: 10.1016/j.oregeorev.2017.01.004

Ludwig, K. R. (2003). *ISOPLOT 3.00: A Geochronological Toolkit for Microsoft Excel*. Berkeley, CA: Berkeley Geochronology Center.

Luo, T., Liao, Q. A., Zhang, X. H., Chen, J. P., Wang, G. C., and Huang, X. (2016). Geochronology and geochemistry of Carboniferous metabasalts in eastern Tianshan, Central Asia: evidence of a back-arc basin. *Int. Geol. Rev.* 58, 756–772. doi: 10.1080/00206814.2015.1114433

Mao, J. W., Goldfarb, R. J., Wang, Y., Hart, C. J., Wang, Z., and Yang, J. (2005). Late Paleozoic base and precious metal deposits, East Tianshan, Xinjiang, China: characteristics and geodynamic setting. *Episodes* 28, 23–30. doi: 10.18814/epiiugs/2005/v28i1/003

Marotta, A. M., Fernandez, M., and Sabadini, R. (1998). Mantle unrooting in collisional settings. *Tectonophysics* 296, 31–46. doi: 10.1016/s0040-1951(98)00134-6

McGee, L. E., and Smith, I. E. M. (2016). Interpreting chemical compositions of small scale basaltic systems: a review. *J. Volcanol. Geotherm. Res.* 325, 45–60. doi: 10.1016/j.jvolgeores.2016.06.007

McKenzie, D., and O'Nions, R. K. (1991). Partial melt distribution from inversion of rare earth element concentrations. *J. Petrol.* 32, 1021–1091. doi: 10.1093/petrology/32.5.1021

Meschede, M. (1986). A method of discriminating between different types of mid-ocean ridge basalts and continental tholeiites with the Nb-Zr-Y diagram. *Chem. Geol.* 56, 207–218. doi: 10.1016/0009-2541(86)90004-5

Mullen, E. D. (1983). $MnO/TiO_2/P_2O_5$: a minor element discriminant for basaltic rocks of oceanic environments and its implications for petrogenesis. *Earth Planet. Sci. Lett.* 62, 53–62. doi: 10.1016/0012-821x(83)90070-5

Pearce, J. A. (2008). Geochemical fingerprinting of oceanic basalts with applications to ophiolite classification and the search for Archean oceanic crust. *Lithos* 100, 14–48. doi: 10.1016/j.lithos.2007.06.016

Pearce, J. A. (2014). Immobile elements fingerprinting of ophiolites. *Elements* 10, 101–108. doi: 10.2113/gselements.10.2.101

Pearce, J. A., and Norry, M. J. (1979). Petrogenetic implications of Ti, Zr, Y and Nb variations in volcanic rocks. *Contrib. Mineral. Petrol.* 69, 33–47. doi: 10.1007/bf00375192

Pearce, J. A. (1982). "Trace element characteristics of lavas from destructive plate boundaries," in *Andesites: Orogenic Andesites and Related Rocks*, ed. R. S. Thorps (New York, NY: John Wiley and Sons), 525–548.

Peccerillo, A., and Taylor, S. R. (1976). Geochemistry of Eocene calc-alkaline volcanic rocks from the Kastamonu area, northern Turkey. *Contrib. Mineral. Petrol.* 58, 63–81. doi: 10.1007/bf00384745

Qin, K. Z., Fang, T. H., Wang, S. L., Zhu, B. Q., Feng, Y. M., Yu, H. F., et al. (2002). Plate tectonics division, evolution and metallogenic settings in eastern Tianshan Mountains. *NW China. Xinjiang Geol.* 20, 302–308.

Rogers, R. D., Kárason, H., and van der Hilst, R. D. (2002). Epeirogenic uplift above a detached slab in northern Central America. *Geol.* 30, 1031–1034. doi: 10.1130/0091-7613(2002)030<1031:euaads>2.0.co;2

Ross, P. S., and Bedard, J. H. (2009). Magmatic affinity of modern and ancient subalkaline volcanic rocks determined from trace-element discriminant diagrams. *Can. J. Earth Sci.* 46, 823–839. doi: 10.1139/e09-054

Rudnick, R. L., and Gao, S. (2014). Composition of the continental Crust. *Treatise Geochem.* 3, 1–51. doi: 10.1016/b0-08-043751-6/03016-4

Saccani, E. (2015). A new method of discriminating different types of post-Archean ophiolitic basalts and their tectonic significance using Th-Nb and Ce-Dy-Yb systematics. *Geosci. Front.* 6, 481–501. doi: 10.1016/j.gsf.2014.03.006

Salters, V. J., and Stracke, A. (2004). Composition of the depleted mantle. *Geochem. Geophys. Geosyst.* 5:Q05004.

Saunders, A. D., Storey, M., Kent, R. W., and Norry, M. J. (1992). Consequences of plume-lithosphere interactions. *Geol. Soc. Lon., Spec. Publ.* 68, 41–60. doi: 10.1144/gsl.sp.1992.068.01.04

Shellnutt, J. G. (2014). The Emeishan large igneous province: a synthesis. *Geosci. Front.* 5, 369–394. doi: 10.1016/j.gsf.2013.07.003

Shen, P., Pan, H. D., and Dong, L. H. (2014). Yandong porphyry Cu deposit, Xinjiang, China geology, geochemistry and SIMS U-Pb zircon geochronology of host porphyries and associated alteration and mineralization. *J. Asian Earth Sci.* 80, 197–217. doi: 10.1016/j.jseaes.2013.11.006

Shervais, J. W. (1982). Ti-V plots and the petrogenesis of modern and ophiolitic lavas. *Earth Planet. Sci. Lett.* 59, 101–118. doi: 10.1016/0012-821x(82)90120-0

Shi, Y., Wang, Y. W., Wang, J. B., Zhou, G. C., Xie, H. J., Li, D. D., et al. (2021). Formation of the Weiya magmatic Fe–Ti oxide deposit and its ore-hosting layered gabbro intrusion, Eastern Tianshan (Xinjiang, NW China). *Ore Geol. Rev.* 28:104003. doi: 10.1016/j.oregeorev.2021.104003

Shu, L. S., Charvet, J., Lu, H. F., and Laurent-Charvet, S. (2002). Paleozoic accretion-collision events and kinematics of deformation in the eastern part of the Southern-Central Tianshan belt. *China. Acta Petrol. Sin.* 76, 308–323. doi: 10.1111/j.1755-6724.2002.tb00547.x

Sun, S. S., and McDonough, W. F. (1989). "Chemical and isotopic systematics of oceanic basalts: implications for mantle composition and processes," in *Magmatism in the Ocean Basins: Geological Society*, Vol. 42, eds A. D. Saunders and M. J. Norry (London: Special Publications), 313–345. doi: 10.1144/gsl.sp.1989.042.01.19

Tanaka, T., Togashi, S., Kamioka, H., Amakawa, H., Kagami, H., and Hamamoto, T. (2000). Jndi-1: a neodymium isotopic reference in consistency with lajolla neodymium. *Chem. Geol.* 168, 279–281. doi: 10.1016/s0009-2541(00)00198-4

Thybo, H., and Nielsen, C. A. (2009). Magma-compensated crustal thinning in continental rift zones. *Nature* 457, 873–876. doi: 10.1038/nature07688

Vermeesch, P. (2006). Tectonic discrimination diagrams revisited. *Geochem. Geophys. Geosyst* 7:Q06017.

Wang, J., Su, Y. P., Zheng, J. P., Gao, S. L., Dai, H. K., Ping, X. Q., et al. (2019). Geochronology and petrogenesis of Jurassic intraplate alkali basalts in the Junggar terrane, NW China: implication for low-volume basaltic volcanism. *Lithos* 324-325, 202–215. doi: 10.1016/j.lithos.2018.11.002

Wang, J. B., Wang, Y. W., and He, Z. J. (2006). Ore deposits as a guide to the tectonic evolution in the East Tianshan Mountains, NW China. *Geol. China* 33, 461–469.

Wang, Y. F., Chen, H. Y., Xiao, B., Han, J. S., Fang, J., Yang, J. T., et al. (2018). Overprinting mineralization in the Paleozoic Yandong porphyry copper deposit, Eastern Tianshan, NW China—Evidence from geology, fluid inclusions and geochronology. *Ore Geol. Rev.* 100, 148–167. doi: 10.1016/j.oregeorev.2017.04.013

Wang, Y. H., Xue, C. J., Liu, J. J., Wang, J. P., Yang, J. T., Zhang, F. F., et al. (2014). Early Carboniferous adakitic rocks in the area of the Tuwu deposit, eastern Tianshan, NW China: slab melting and implications for porphyry copper mineralization. *J. Asian Earth Sci.* 103, 1–18.

Wang, Y. H., and Zhang, F. F. (2016). Petrogenesis of early Silurian intrusions in the Sanchakou area of Eastern Tianshan, Northwest China, and tectonic implications: geochronological, geochemical, and Hf isotopic evidence. *Int. Geol. Rev.* 58, 1–17.

Wilson, M. (1989). *Igneous Petrogenesis-A Global Tectonic Approach*. London: Unwin Hyman, 466.

Wood, D. A. (1980). The application of a Th-Hf-Ta diagram to problems of tectonomagmatic classification and to establishing the nature of crustal contamination of basaltic lavas of British Tertialy volcanic province. *Earth Planet. Sci. Lett.* 50, 11–30. doi: 10.1016/0012-821x(80)90116-8

Wu, C. Z., Zhang, Z. Z., Zaw, K., Della-Pasque, F., Tang, J. H., Zheng, Y. C., et al. (2006). Geochronology, geochemistry and tectonic significances of the Hongyuntan granitoids in the Qoltag area, Eastern Tianshan. *Acta Petrol. Sin.* 22, 1121–1134.

Wu, Y. S., Zhou, K. F., Li, N., and Chen, Y. J. (2017). Zircon U-Pb dating and Sr-Nd-Pb-Hf isotopes of the ore-associated porphyry at the giant Donggebi Mo deposit, Eastern Tianshan, NW China. *Ore Geol. Rev.* 81, 794–807. doi: 10.1016/j.oregeorev.2016.02.007

Xia, L., and Li, X. (2019). Basalt geochemistry as a diagnostic indicator of tectonic setting. *Gondwana Res.* 65, 43–67. doi: 10.1016/j.gr.2018.08.006

Xiao, B., Chen, H. Y., Hollings, P., Han, J. S., Wang, Y. F., Yang, J. T., et al. (2017). Magmatic evolution of the Tuwu–Yandong porphyry Cu belt, NW China: constraints from geochronology, geochemistry and Sr–Nd–Hf isotopes. *Gondwana Res.* 43, 74–91. doi: 10.1016/j.gr.2015.09.003

Xiao, W. J., Han, C. M., Yuan, C., Sun, M., Lin, S. F., Chen, H. L., et al. (2008). Middle Cambrian to Permian subduction-related accretionary orogenesis of northern Xinjiang, NW China: implications for the tectonic evolution of Central Asia. *J. Asian Earth Sci.* 32, 102–117. doi: 10.1016/j.jseaes.2007.10.008

Xu, J. F., Shinjo, R., Defant, M. J., Wang, Q., and Rapp, R. P. (2002). Origin of Mesozoic adakitic intrusive rocks in the Ningzhen area of east China: partial melting of delaminated lower continental crust? *Geol* 30, 1111–1114. doi: 10.1130/0091-7613(2002)030<1111:oomair>2.0.co;2

Yang, F. Q., Mao, J. W., Bierlein, F. P., Pirajno, F., Zhao, C. S., Ye, H. S., et al. (2009). A review of the geological characteristics and geodynamic mechanisms of Late Paleozoic epithermal gold deposits in North Xinjiang, China. *Ore Geol. Rev.* 35, 217–234. doi: 10.1016/j.oregeorev.2008.09.003

Zhang, D. Y., Zhou, T. F., Yuan, F., Xiao, W. J., White, N. C., Deng, Y. F., et al. (2015). Petrogenesis and mineralization potential of a granite porphyry intrusion beneath the Baishan Mo deposit, Eastern Tianshan, NW China. *J. Asian Earth Sci.* 113, 254–265. doi: 10.1016/j.jseaes.2015.05.002

Zhang, M. G., Li, C., Fu, P., Hu, P., and Ripley, E. M. (2011). The Permian Huangshanxi Cu–Ni deposit in western China: intrusive–extrusive association,

ore genesis, and exploration implications. *Mineral. Deposita* 46, 153–170. doi: 10.1007/s00126-010-0318-3

Zhang, W. F., Chen, H. Y., Han, J. S., Zhao, L. D., Huang, J. H., Yang, J. T., et al. (2016). Geochronology and geochemistry of igneous rocks in the Bailingshan area: implications for the tectonic setting of late Paleozoic magmatism and iron skarn mineralization in the eastern Tianshan, NW China. *Gondwana Res.* 38, 40–59. doi: 10.1016/j.gr.2015.10.011

Zhang, W. F., Chen, H. Y., Jiang, H. J., Lu, W. J., Liang, P., Xu, C., et al. (2017). Geochronology, geochemistry and petrogenesis of granitoids in the Duotoushan Fe-Cu deposit, eastern Tianshan, Xinjiang province: implications on tectonic setting of late Paleozoic magmatism. *Geotech. Metall.* 41, 1171–1191.

Zhang, W. F., Chen, H. Y., Peng, L. H., Zhao, L. D., Huang, J. H., Lu, W. J., et al. (2018a). Discriminating hydrothermal fluid sources using tourmaline boron isotopes: example from Bailingshan Fe deposit in the Eastern Tianshan, NW China. *Ore Geol. Rev.* 98, 28–37. doi: 10.1016/j.oregeorev.2018.05.015

Zhang, W. F., Chen, H. Y., Peng, L. H., Zhao, L. D., Lu, W. J., Zhang, Z. J., et al. (2018b). Ore genesis of the Duotoushan Fe-Cu deposit, Eastern Tianshan, NW China: constraints from ore geology, mineral geochemistry, fluid inclusion and stable isotopes. *Ore Geol. Rev.* 100, 401–421. doi: 10.1016/j.oregeorev.2017.02.021

Zhang, X. H., Huang, X., Chen, J. P., Liao, Q. A., and Duan, X. F. (2012). Stratigraphic sequence of carboniferous marine volcanic-deposit rock and its geological age in Juotage Area, Eastern Tianshan. *Earth Sci.-J. China Univ. Geosci.* 6, 1305–1314.

Zhao, L. D., Chen, H. Y., Hollings, P., and Han, J. S. (2019). Tectonic transition in the Aqishan-Yamansu belt, Eastern Tianshan: constraints from the geochronology and geochemistry of Carboniferous and Triassic igneous rocks. *Lithos* 344-345, 247–264. doi: 10.1016/j.lithos.2019.06.023

Zheng, J. H., Mao, J. W., Yang, F. Q., Liu, F., and Zhu, Y. F. (2015). The post-collisional Cihai iron skarn deposit, eastern Tianshan, Xinjiang, China. *Ore Geol. Rev.* 67, 244–254. doi: 10.1016/j.oregeorev.2014.12.006

Zhou, M. F., Zhao, J. H., Jiang, C. Y., Gao, J. F., Wang, W., and Yang, S. H. (2009). OIB-like, heterogeneous mantle sources of Permian basaltic magmatism in the western Tarim Basin, NW China: implications for a possible Permian large igneous province. *Lithos* 113, 583–594. doi: 10.1016/j.lithos.2009.06.027

Zhou, T. F., Yuan, F., Zhang, D. Y., Fan, Y., Liu, S., Peng, M. X., et al. (2010). Geochronology, tectonic setting and mineralization of granitoids in Jueluotage area, eastern Tianshan, Xinjiang. *Acta Petrol. Sin.* 26, 478–520.

Conflict of Interest: The authors declare that the research was conducted in the absence of any commercial or financial relationships that could be construed as a potential conflict of interest.

The reviewer JH declared a past co-authorship with one of the authors WZ.